



Original article



Improved charge transfer and enhanced visible light photocatalytic activity of Bi₂O₃@Fe-MOF for degradation of Rhodamine B and Triclopyr

Anuradha Sharma^a, Muhammad Tahir^b, Tansir Ahamad^{c,*}, Naveen Kumar^{a,*}, Shankar Sharma^a, Monika Kumari^a, M.A. Majeed Khan^d, Sourbh Takhur^e, Pankaj Raizada^f

^a Department of Chemistry, Maharshi Dayanand University, Rohtak 124001, India

^b Chemical and Petroleum Engineering Department, UAE University, P.O. Box 15551, Al Ain, United Arab Emirates

^c Department of Chemistry, College of Science, King Saud University, Saudi Arabia

^d College of Science, King Saud University, Saudi Arabia

^e Department of Organic Chemistry, Bioorganic Chemistry and Biotechnology, Silesian University of Technology, B. Krzywoustego 4, 44-100 Gliwice, Poland

^f School of Advanced Chemical Sciences, Faculty of Basic Sciences, Shoolini University, Solan, Himachal Pradesh 173212, India

ARTICLE INFO

Keywords:

Degradation
Photocatalysis
Composite
MOF

ABSTRACT

Objectives: Metal organic frameworks (MOFs) composites, integrated with metal oxides augment the inherent characteristics of the original frameworks. Present study aims to investigate and assess the potential of Bi₂O₃@Fe-MOF composites in efficient photocatalytic degradation of two distinct organic pollutants, namely Rhodamine B (RhB) dye and Triclopyr (TC) pesticide.

Methods: A series of Bi₂O₃@Fe-MOF was synthesized by changing the Fe: Bi molar ratios and following the solvothermal method. Fabricated materials were analyzed primarily for crystalline arrangements, morphology features and chemical compositions, band gap energies, functional moieties, recombination of charge carriers, and surface charge. These assessments were carried out with the different advanced techniques including XRD, FTIR, FESEM and EDX, UV-Vis DRS, PL, and Zeta potential analysis. The synthesized composites were studied for their ability in photocatalytic breakdown of RhB and TC under visible light irradiation. The pseudo first order kinetic model is implemented to study the degradation kinetics of the pollutants. Trapping experiments were performed to determine the reactive species responsible for the degradation reaction.

Results and conclusions: The study showed that the crystalline nature, morphology, and optical absorbance of the prepared composites changed with Fe:Bi molar ratio. The degradation efficiency of Bi₂O₃@Fe-MOF-3 for RhB and TC was 91.79% and 88.42%, respectively, in 120 min, making it the most effective synthesized material. The pseudo-first-order kinetic model was in good agreement with the experimental data. The trapping experiments revealed that hydroxyl radicals ([•]OH) were the main contributors to the degradation reaction.

This study concluded that Bi₂O₃@Fe-MOF composites are promising photocatalysts for the degradation of organic pollutants. The highest photocatalytic performance of Bi₂O₃@Fe-MOF-3 is attributed to the connected interfaces between Bi₂O₃ and Fe-MOF phases, which facilitate effective charge injections and separation.

1. Introduction

Bi₂O₃ has shown great potential as a photocatalyst for the degradation of organic pollutants in water, due to its environmental friendliness and visible light activity. The hybridization of Bi-6s and O-2p orbitals in Bi₂O₃ provides a highway for the movement of valence band up which is beneficial for the transfer of electrons from low energy valence band to high energy conduction band. Moreover, the wide and delocalized bands

are favorable for the diffusion of photoinduced charge carriers (Chen et al., 2015). Bulk Bi₂O₃ exist in five different crystalline phases, of which α and δ are the most stable. The other three phases (β , γ , and ω) are metastable. The narrow band gap of β -Bi₂O₃ (2.8 eV) allows it to be excited by visible light, making it a p-type oxide semiconductor (Hu et al., 2018). However, there are difficulties including lower solar energy utilization, fast recombination, and recovery issues during recycling that results limited practical applications. Consequently, it is

Peer review under responsibility of King Saud University.

* Corresponding authors.

E-mail addresses: tansirahamad@gmail.com (T. Ahamad), naveenkumar.chem@mdurohtak.ac.in (N. Kumar).

<https://doi.org/10.1016/j.jksus.2023.102922>

Received 18 May 2023; Received in revised form 3 September 2023; Accepted 27 September 2023

Available online 30 September 2023

1018-3647/© 2023 The Authors. Published by Elsevier B.V. on behalf of King Saud University. This is an open access article under the CC BY-NC-ND license (<http://creativecommons.org/licenses/by-nc-nd/4.0/>).

required to improve the photocatalytic efficiency by different methods among which heterostructure formation has been found the most effective and efficient method (Chawla et al., 2023; Dutta et al., 2023; Khan et al., 2023).

MOFs have rapidly progressed in their ability for the effective adsorption and degradation of various types of hazardous water contaminants, due to their high surface area, tunable porosity along with thermal and chemical stability. There are several studies that have reported excellent enhancement in the photocatalytic efficiency of the composite materials of MOFs with other semiconductors like ZnO, TiO₂, ZnFe₂O₄, WO₃, and BiVO₄ for the removal of organic contaminants. A MOF-based magnetic nanocatalyst with Fe₃O₄ was applied to remove methyl orange (Ghouchian et al., 2021) and exhibited magnetic separable characteristics. TiO₂@MIL-101 (Cr) composites were designed for photodegradation of Bisphenol A wherein improved features were obtained with reduced recombination of charge carriers (Tang et al., 2020). Encased Bi₂O₃ nanoparticles into the pores of Cu-MOF exhibited excellent photodegradation efficiency towards nuclear fast red dye (Guo et al., 2016). The removal efficiency of the composite materials depends upon the type of the semiconductors as well as the nature of heterostructures and migration of active species across the interfacial layers. Generally, Type-II and Z-scheme mechanisms of charge migration are followed in photocatalytic reactions. Fabrication of Z-scheme heterojunctions has been reported as the feasible strategy to enhance the migration efficiency of the photoelectrons. In Z-scheme, low resistance transfer of electrons is allowed between the semiconductors and smaller change in Gibbs free energy is required as compared to the Type-II mechanism. Therefore, stronger ability is achieved in Z-scheme junctions to facilitate the various redox photoreactions (Zhong et al., 2022). A Z-scheme Bi₂WO₆/Ni-MOF heterostructure with enhanced photocatalytic activity for methylene blue degradation was constructed by wrapping Bi₂WO₆ on Ni-MOF sheets (Cheng et al., 2022). Ti-MOF/Ag/NiFeLDH composites displayed outstanding degradation activity for organic dye RhB and an antibiotic Levofloxacin where constructed heterostructures enhanced the catalytic efficiency following the Z-scheme charge movement mechanism (Liu et al., 2021).

Among bountiful metal organic frameworks, Fe-MOFs are extensively advantageous being less toxic and abundant presence of iron in the earth's crust. Additional benefits include excellent interfacial charge transfer properties, unsaturated metal centers of high catalytic activity, and lower band gap energies as compared to the other MOFs due to which these can be easily excited under visible light (Joseph et al., 2021). Above literature inspired us to fabricate Z-scheme Bi₂O₃@Fe-MOF and investigated against decontamination of two different organic pollutants namely Rhodamine B (RhB) and Triclopyr (TC). Herein, the nanocomposites were synthesized by solvothermal method and optimal ratio of the constituents in the composites (Fe: Bi) was determined. Possible photodegradation mechanism was also speculated. This study may be an efficient and sustainable method for the waste water decontamination.

2. Experimental section

2.1. Chemicals used

Bismuth nitrate [Bi(NO₃)₃·5H₂O, 99.9%], Ferric nitrate [Fe(NO₃)₃·9H₂O, 99.9%], Terephthalic acid (1, 4 benzenedicarboxylic acid, 98%), N, N dimethylformamide (DMF, 99.5%), and HNO₃ were taken from CDH chemicals. Urea [NH₂CO NH₂, 99.5%] was utilized as the fuel. Sigma Aldrich, India, was the supplier of the model contaminants Rhodamine B and Triclopyr.

2.2. Fabrication of Bi₂O₃ and Bi₂O₃@Fe-MOF nanocomposites photocatalysts

2.2.1. Bi₂O₃

Bi₂O₃ was prepared by the simple and efficient solution combustion method following the literature with slight modifications (Astuti et al., 2020b). First, calculated amount of (4.8507 g) of bismuth nitrate was blended with appropriate quantity of urea, which is used as the fuel. To this mixture, 5 ml of 1 M HNO₃ was introduced and thoroughly stirred on a hot plate to achieve a homogeneous and consistent mixture. To avoid the oxo-nitride formation and precipitation of Bi ions, it is necessary to use an acidic solvent which is usually nitric acid in distilled water (Iyyapushpam et al., 2013), and the same was used in the present procedure. The obtained solution was subjected to a thermal treatment a preheated muffle furnace set at 400 °C for a duration of 30 min. This process led to the rapid dehydration and combustion of the solution, releasing gases. The resultant product was allowed to cool at ambient room temperature. The resulting solid powder was pulverized and collected for subsequent characterization and experimentation.

2.2.2. Fe-MOF

Fe-MOF was fabricated using a hydrothermal procedure reported previously with slight modifications (Li et al., 2020; Yan et al., 2019). Ferric nitrate (4 mmol, 1.616 g) was dissolved in 15 ml DMF and stirred for 10 min. Another beaker contained terephthalic acid (2 mmol, 0.332 g) again in 15 ml DMF and stirred for the same time. The obtained two clear solutions were mixed and stirred for an additional 20 min using a magnetic stirrer. The mixture was then transferred to an autoclave and subjected to a temperature of 120 °C for 24 h. The product was isolated by filtration and then washed with DMF many times to remove the unreacted moieties. Then the compound was dried overnight at 80 °C to get the final Fe-MOF.

2.2.3. Bi₂O₃@Fe-MOF composites

Pre-calculated stoichiometric quantities of Bi₂O₃ powder were incorporated corresponding to the distinct molar ratios of (Fe: Bi) into the ferric nitrate solution (Chen et al., 2020). Similar procedure was then followed for further steps until autoclave placed at 120 °C for 24 h. Three composites in 1:0.3, 1:0.05, and 1:0.1 were obtained and named as Bi₂O₃@Fe-MOF-1, Bi₂O₃@Fe-MOF-2, and Bi₂O₃@Fe-MOF-3, respectively.

2.3. Characterizations

To analyze the phase and structural attributes of the produced materials, SmartLab 3 kW-Rigaku instrument was used to obtain their high-quality XRD patterns. To access morphology, the field emission scanning electron microscopy technique (FESEM) (7610F Plus/JEOL) was employed. Energy dispersive x-ray spectroscopy (EDX) coupled with FESEM was used to confirm the elemental composition. Optical properties and band gap characteristics were investigated using Shimadzu-3600 plus double beam UV-vis spectrophotometer. The separation of photogenerated charge carriers was studied by Photoluminescence (PL) spectroscopy. The spectra were acquired using a Hitachi F-7000 fluorescence spectrophotometer. Furthermore, the zeta potential (ζ) of the synthesized materials was measured using a (Zetasizer Ver. 7.13) analyzer.

2.4. Photocatalytic activity procedure

To evaluate the photocatalytic degradation ability of the synthesized compounds, Rhodamine B dye and Triclopyr pesticide were employed as the representative pollutants. The degradation experiment involved the addition of 10 mg of the photocatalyst into a 100 ml aqueous solution of the pollutant (10 ppm). Subsequently the mixture was stirred under dark conditions until adsorption-desorption equilibrium was reached. The

stirring process was continued for 60 min at a controlled temperature of 25 °C. After that, a visible light lamp (250 W) was turned on and oxygen was supplied continuously. At regular intervals, approximately 5 ml of the experimental solution was taken out for centrifugation, facilitating the separation of photocatalyst from the solution. The remaining concentration of the dye and pesticide in the collected solution was determined using a double beam UV–visible spectrophotometer by measuring the absorbance at their respective wavelengths of maximum absorption (553 and 295 nm respectively). The percentage degradation efficiency (η) was calculated utilizing the following equation:

$$\eta = \frac{C_0 - C_t}{C_0} * 100$$

where C_0 and C_t represent the concentration of organic pollutant at the initial time and after time t , respectively.

Furthermore, the impact of pH on the degradation process was investigated across the pH range of 3–11. To understand the involvement of reactive oxygen species, scavenger's studies were conducted, aimed at evaluating the various reactive species.

3. Results and discussion

3.1. XRD analysis

The crystalline structure of the synthesized materials was studied by recording the high quality XRD patterns (Fig. 1). XRD patterns were provided the evidence of the crystalline nature of the synthesized materials as depicted in the Fig. 1. The diffraction peaks obtained at 2θ values 5.06°, 8.90°, 10.20°, 16.40°, 18.84°, 24.22°, and 35.74° agree with the previously reported works (Hao et al., 2022; Yan et al., 2019) and confirm the successful synthesis of Fe-MOF. Sharp peaks below 10° indicated the formation of well crystalline MOF material. For Bi_2O_3 , the obtained diffraction positions were in agreement with the β -tetragonal Bi_2O_3 phase (PDF NO. 27-50). The distinct peaks characteristic of Fe-

MOF are also obtained in the patterns of the composite materials with Bi_2O_3 . This observation indicates that the structural integrity of the Fe-MOF framework remains unaffected after the incorporation of Bi_2O_3 nanoparticles. To determine the crystallite sizes of these materials, Scherrer's equation was employed (Kumari et al., 2020). The calculated sizes were found to be 10.24, 8.85, 9.10, 8.85, 9.10 nm for Bi_2O_3 , Fe-MOF, Bi_2O_3 @Fe-MOF-1, Bi_2O_3 @Fe-MOF-2, and Bi_2O_3 @Fe-MOF-3, respectively.

3.2. FESEM and EDX

Surface micrographs of the synthesized samples were obtained using FESEM to study their morphology. Fig. 2A depicts FESEM images of Bi_2O_3 , Fe-MOF and Bi_2O_3 @Fe-MOF-3 composite. The agglomeration of pure Bi_2O_3 nanoparticles was possibly caused by electrostatic interactions, resulting in an irregular morphology (Koli et al., 2021). Fe-MOF material exhibited the rough surface with pores which is favorable for binding adsorbate molecules. The material was composed of a numerous accumulated nanoparticle, resulting in void spaces/sites i.e. pores among them. Within the composite material, similar micrographs depicted the attachment of Bi_2O_3 nanoparticles to the surface of Fe-MOF. The EDX spectrum in Fig. 2B shows all the relevant peaks for the constituents of the synthesized materials, with no additional peaks detected. Further, investigation into the elemental distribution through elemental mapping of the synthesized compounds further supported the uniform distribution of the elements.

3.3. UV–Vis DRS

UV visible spectra were recorded to study the optical response and band gap energies of the prepared materials. As shown in the Fig. 3A, Bi_2O_3 shows an absorption edge at a shorter wavelength (414 nm) than Fe-MOF (855 nm). Absorption bands of the composites were detected in the region 800–850 nm. The band gap energies were evaluated

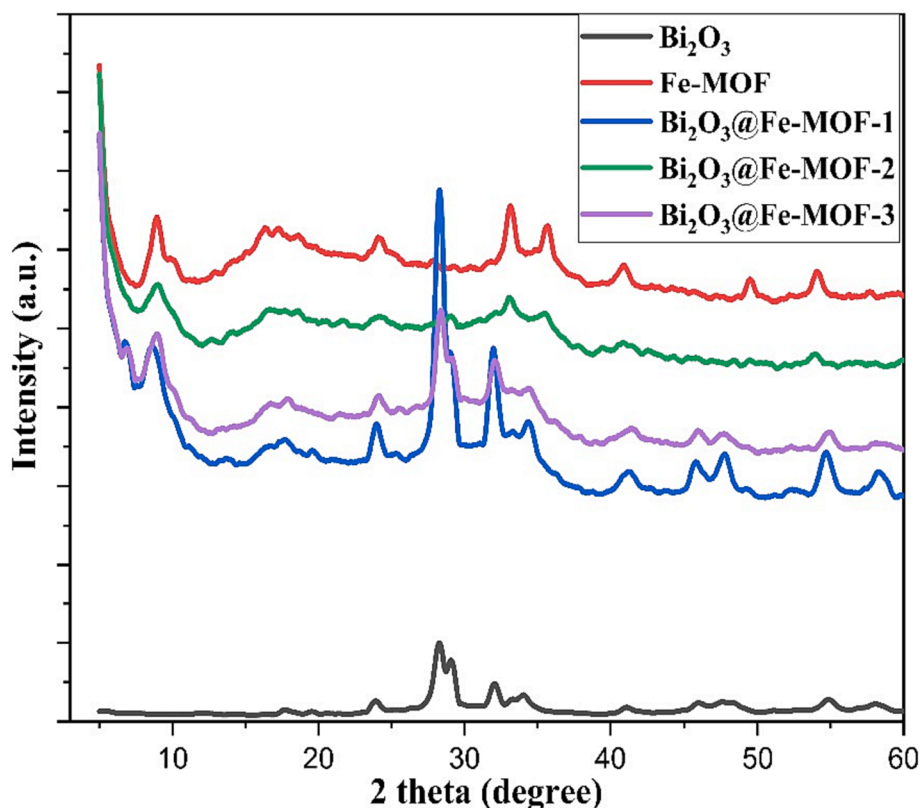


Fig. 1. XRD patterns of Fe-MOF, Bi_2O_3 , and Bi_2O_3 @Fe-MOF composites.

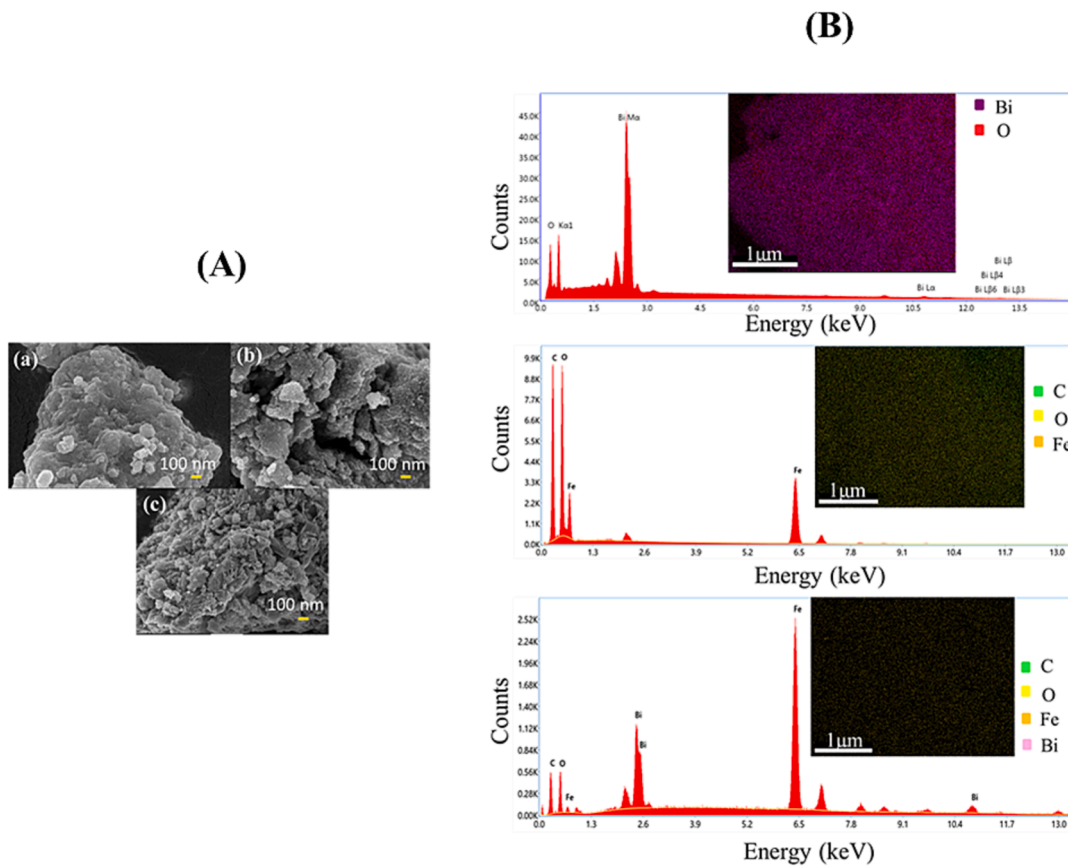


Fig. 2. (A) FESEM images of (a) Bi_2O_3 , (b) Fe-MOF, and (c) Bi_2O_3 @Fe-MOF-3 composite and (B) EDX constitution and elemental mapping of the synthesized compounds.

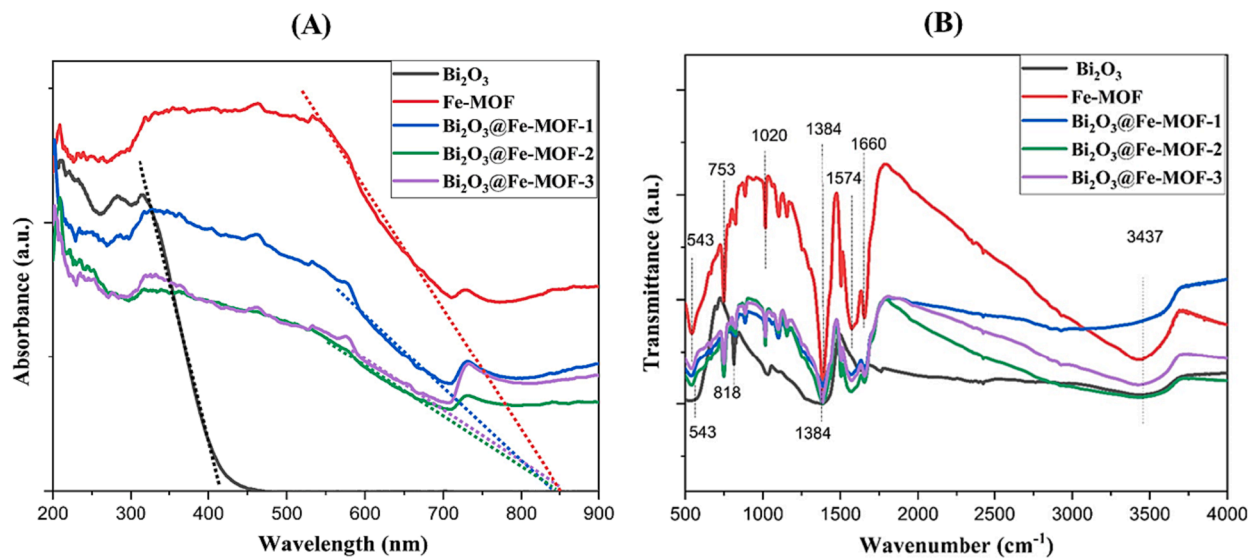


Fig. 3. (A) UV-Vis DRS spectra of all the synthesized nanomaterials and (B) FTIR spectra of all the synthesized materials.

according to the relation:

$$E_g = \frac{1240}{\lambda_g}$$

where λ_g represents the main absorption edge wavelength in nm. The calculated values of band gaps were 2.99, 1.45, 1.48, 1.47, and 1.46 eV for Bi_2O_3 , Fe-MOF, Bi_2O_3 @Fe-MOF-1, Bi_2O_3 @Fe-MOF-2, and

Bi_2O_3 @Fe-MOF-3, respectively. It is observed that with increase in Bi content in MOF, band gap values were gradually increased.

3.4. FTIR

Structures of the fabricated materials were further confirmed with FTIR spectra recorded in the range 500–4000 cm^{-1} (Fig. 3B). The Fe-MOF has characteristic peaks at 543, 753, 1020, 1384, 1574, and

1660 cm^{-1} . The peak appeared at 543 cm^{-1} is due to the Fe—O bond vibration (Gecgel et al., 2019). Peak 753 cm^{-1} corresponds to the C—H bond bending vibration of the benzene ring and at 1020 cm^{-1} is assigned to the C—O—C bond. Peaks obtained at 1384 and 1574 cm^{-1} confirmed the carboxyl group while at 1660 cm^{-1} is due to the C=O bond stretching vibration. For Bi_2O_3 , vibrational band at 543 cm^{-1} is originated from Bi—O bond while at 818 cm^{-1} belongs to the vibration of Bi—O—Bi bonds (Motakef-Kazemi and Yaqoubi, 2020; Yang et al., 2018). The peak at 1384 cm^{-1} corresponds to the stretching vibration of Bi—O bond (Astuti et al., 2020a). In addition, peak at 3437 cm^{-1} indicates the stretching vibration of O—H bond of the adsorbed water molecules (Yang et al., 2018). All the characteristic peaks of Fe-MOF were retained in the $\text{Bi}_2\text{O}_3/\text{Fe-MOF}$ composites indicating the existence of stable crystal structure of Fe-MOF in the composites.

3.5. PL spectra

It is widely recognized that the PL signals arise due to the recombination of electron-hole pair's within semiconductor materials (Sharma et al., 2021). Intensity of a peak in a photoluminescence spectrum is directly related to the rate of electron-hole recombination in the sample being studied. In the sample with high recombination rates, the PL peak has a high emission intensity, indicating that excited electrons and holes are recombined rapidly and vice versa (Fan et al., 2014). PL emission spectra of the different synthesized materials were recorded at room temperature (Fig. 4). Among all the synthesized samples, Bi_2O_3 exhibited the highest emission intensity i.e. maximum recombination of charge carriers while $\text{Bi}_2\text{O}_3/\text{Fe-MOF-3}$ had lowest emission intensity in the spectrum as shown in the inset Fig. 4. Minimum peak intensity of the composite $\text{Bi}_2\text{O}_3/\text{Fe-MOF-3}$ indicated the highest separation of the photogenerated electron holes pairs and hence the maximum photocatalytic efficiency of this material towards degradation of organic pollutants.

4. Photodegradation evaluation

4.1. Catalytic efficiency and degradation kinetics

The ability of the synthesized materials to degrade RhB and TC under visible light irradiation was studied. The results obtained are depicted in

the Fig. 5(Aa and Ba) for both the pollutants, respectively. It can be seen that Bi_2O_3 exhibited lower adsorption and photodegradation activity for both the pollutants (50.87% for RhB and 68.89% for TC in 120 min). Fe-MOF showed strong adsorption capacity under dark conditions and moderate photodegradation activity for both the pollutants, respectively. With Fe-MOF, removal efficiencies obtained were 78.99 and 77.04% for RhB and TC, respectively. Composites $\text{Bi}_2\text{O}_3/\text{Fe-MOF}$ showed lower adsorption capacity for both the pollutants which may be ascribed to the decreased surface areas of the composite materials as compared to the Fe-MOF (Tang et al., 2020). However, the photocatalytic activity of the $\text{Bi}_2\text{O}_3/\text{Fe-MOF}$ composites was found significantly increased than the both pristine Bi_2O_3 and Fe-MOF. Out of all the composites, $\text{Bi}_2\text{O}_3/\text{Fe-MOF-3}$ exhibited the highest degradation efficiency for both the pollutants (91.79 and 88.42% respectively in 120 min). The enhanced photoactivity of the composite materials is attributed to the $\text{Bi}_2\text{O}_3/\text{Fe-MOF}$ heterojunctions owing to which effective separation and movement of the charge carriers become successful (Wu et al., 2022). Further, Fig. 5(Ab and Bb) showed the photodegradation kinetics of both the pollutants. Langmuir-Hinshelwood model was employed to study the kinetics of degradation where pseudo-first-order reaction kinetics was followed (Danish and Muneer, 2021). Curve fitting of this model was utilized to evaluate rate constants and regression constants that are tabulated in Tables S1 & S2.

4.2. pH of the medium and scavengers study

The pH of the initial solution can affect the number of available adsorption sites, surface charge, and hence binding and reactivity of the photocatalyst towards organic pollutants. To examine the effect of pH conditions for the synthesized compounds, initial solution pH was selected 3, 5 (acidic), 7 (neutral), and 9, 11 (basic). Fig. 6(Aa and Ba) depict the degradation in different pH mediums of both the pollutants (RhB and TC), respectively. For RhB, when pH increased from 3 to 5, degradation also increased up to ~99% in 120 min. Further, rise of pH from 7 to 11 lead gradual decrease in photocatalytic activity (Fig. 6Aa). This can be explained by the electrical charges of RhB molecules and the electrostatic interactions with the photocatalyst surface that dominate in the adsorption process. In highly acidic environment (pH = 3), catalyst surface becomes protonated (zeta potential = + 2.48 mV) and repels away the cationic molecules of the dye. Thus, degradation efficiency

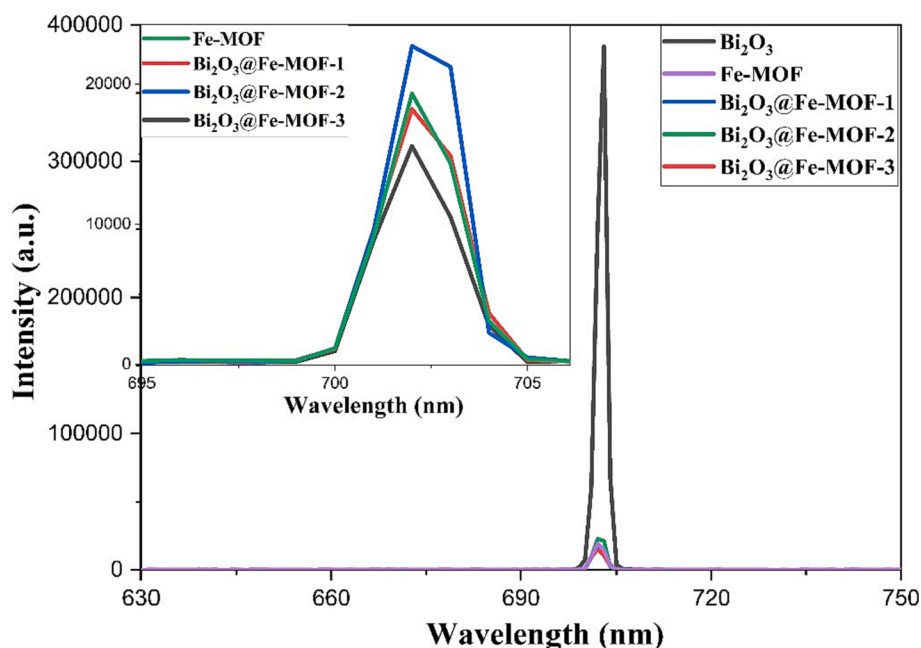


Fig. 4. Photoluminescence spectra of Bi_2O_3 , Fe-MOF, and $\text{Bi}_2\text{O}_3/\text{Fe-MOF}$ composites.

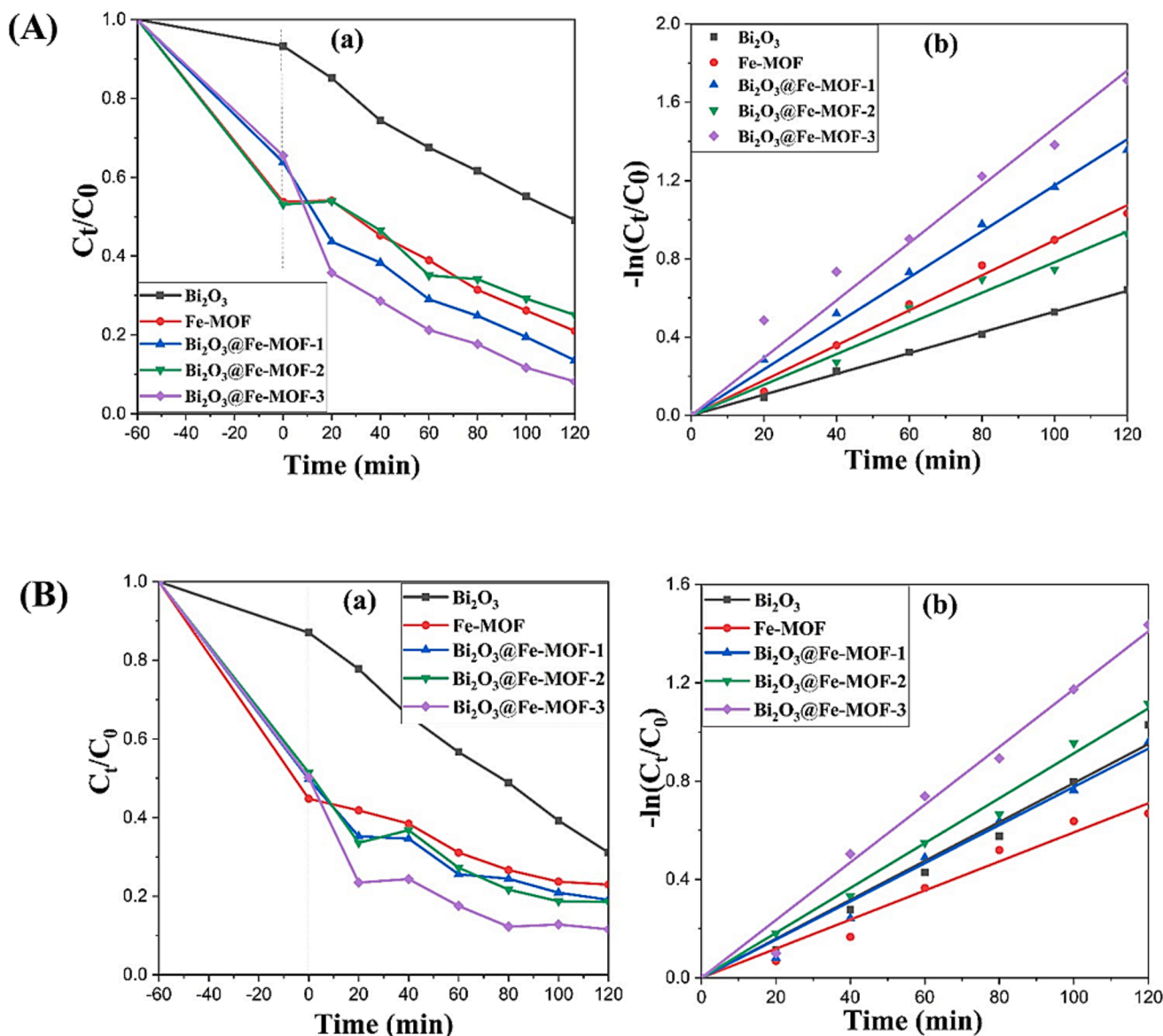


Fig. 5. (A) (a) Photocatalytic removal and (b) kinetic study of RhB degradation and (B) (a) Photocatalytic removal and (b) Degradation kinetics of TC by prepared samples.

decreases at pH = 3 than pH = 5. Further, under acidic conditions, the existence of H^+ ions result in a huge production of $\cdot\text{OH}$ radicals, hence resulting in a high photodegradation rate of organic pollutants as compared to the neutral media (Nguyen Thi et al., 2021). Moderate degradation was obtained at pH = 7. At higher pH from 9 to 11, cationic dye is adsorbed more strongly on the negatively charged catalyst surface (zeta potential = -13.4 mV) and more adsorption of the dye molecules effectively shields the surface of the catalyst and prevented the contact of the catalytic surface with light, resulting in a decreased photocatalytic efficiency (Nguyen et al., 2018).

On the other hand, Triclopyr showed maximum removal under neutral conditions and decreased activity in both acidic and alkaline conditions (Fig. 6Ba). This can be attributed to the charge of the photocatalyst surface and acid dissociation constant of Triclopyr ($\text{pK}_a = 2.93$) under different pH values of the solution. At acidic pH, pesticide molecules are more likely to exist in their undissociated form which result in lesser adsorption and photocatalytic activity (Poulios et al., 1998). In basic pH conditions, the removal efficiency decreased due to the repulsive forces between the negatively charged catalyst and the anions. In addition, hindrance caused by the excess OH^- ions also

prevents the absorption of light and generation of the reactive species that are needed for an efficient degradation of the pollutants.

Trapping experiments for the different reactive species were performed to examine the role of these species in the photodegradation reaction. The scavengers like ethylene diamine tetra-acetic acid (EDTA), p-benzoquinone (BQ) and isopropanol (IPA) were used to examine the involved reactive species. BQ, IPA and EDTA are highly reactive to superoxide anion radicals ($\cdot\text{O}_2^-$), hydroxyl radicals ($\cdot\text{OH}$), and holes respectively. Fig. 6(Ab and Bb) clearly shows that the presence of all scavengers hinders the decomposition of the organic pollutants. EDTA exhibits the highest scavenging performance with maximum decline in efficiency of the photocatalyst against both RhB and TC, suggesting major role of holes species in the reaction mechanism for oxidation of pollutants under visible light irradiation. Whereas, lesser effect on degradation rate by IPA and BQ for RhB, suggested lower participation of hydroxyl radicals and superoxide anion radicals in the degradation process. On the other side, the reaction rate of photocatalytic oxidation of TC was significantly inhibited by both IPA and BQ addition, indicating that hydroxyl radicals ($\cdot\text{OH}$) and superoxide anion radicals ($\cdot\text{O}_2^-$) also played their role in the photodegradation process of the pollutant.

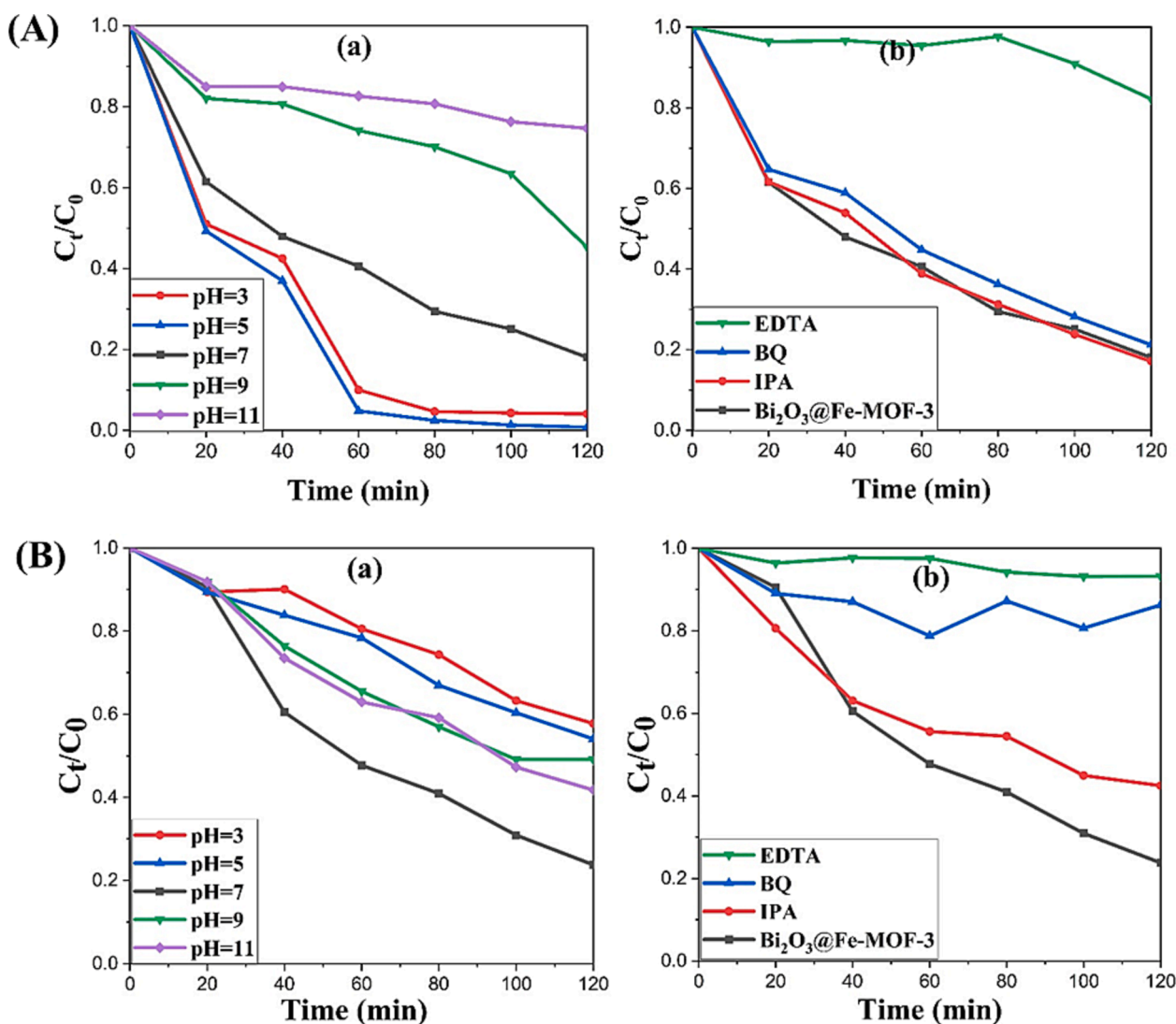


Fig. 6. Photocatalytic decontamination of (A) RhB and (B) TC involving (a) effect of different pH mediums and (b) effect of addition of different scavengers on $\text{Bi}_2\text{O}_3/\text{Fe-MOF-3}$.

4.3. Mechanism of degradation

The efficiency of photocatalysis in composite structures depends on the production, separation, and migration of electron-hole pairs (Hu et al., 2023). On the basis of energy level diagram, possible photocatalytic mechanism for degradation of organic pollutants with $\text{Bi}_2\text{O}_3/\text{Fe-MOF}$ composites is illustrated in the Fig. 7. The valence band and conduction band of Bi_2O_3 lies at higher positive potentials than the LUMO and HOMO potentials of Fe-MOF (Hao et al., 2022; Lan et al., 2022). Therefore, the Z-scheme charge transfer mechanism is a possible explanation for the observed results (Raizada et al., 2019). Under the visible light illumination, both the materials i.e. Bi_2O_3 and Fe-MOF get excited and generate electrons and holes respectively. The photo-generated electrons in the higher energy conduction band of Bi_2O_3 migrate to the low energy valence band of Fe-MOF owing to the internal field at the heterojunction interface. The quick combination of these electrons with the holes species of Fe-MOF, boosts up the interfacial separation of charged carriers. Ultimately, electrons in the conduction band of Fe-MOF and holes in the valence band of Bi_2O_3 remain reserved. According to the literature reported values of the conduction band of Fe-MOF being more negative than the O_2/O_2^- reduction potential (-0.33 eV), the electrons in LUMO of Fe-MOF can transform the O_2 molecules into O_2^- radicals. In the similar manner, holes in the valence band of

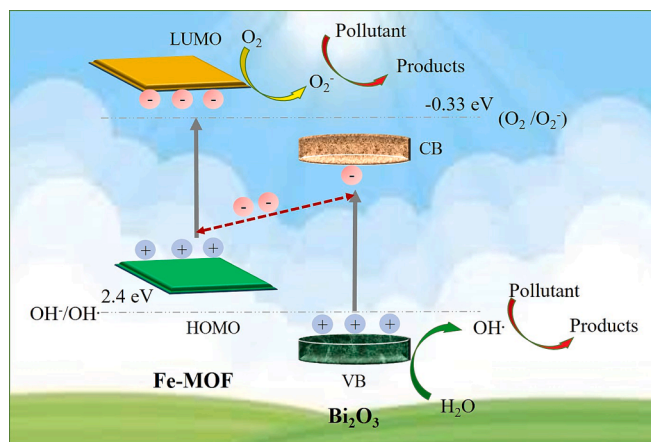


Fig. 7. Proposed Z-scheme photocatalytic charge transfer mechanism of $\text{Bi}_2\text{O}_3/\text{Fe-MOF}$ composites for degradation of organic pollutants.

Bi_2O_3 produce $\cdot\text{OH}$ radicals from H_2O molecules oxidation [$\text{H}_2\text{O}/\cdot\text{OH}$ (2.4 eV)] as indicated by their respective redox potential values. The reactive species thus produced ($\cdot\text{O}_2$ and $\cdot\text{OH}$ radicals) then decompose the targeted organic pollutant molecules. Therefore, the improvement in the photocatalytic performance of the composite $\text{Bi}_2\text{O}_3@$ Fe-MOF is ascribed to the effective generation and separation of photogenerated charge carriers at the Z-scheme heterojunctions.

5. Conclusion

The energy efficient solvothermal technique was adopted to synthesize a series of $\text{Bi}_2\text{O}_3@$ Fe-MOF composites. The synthesized materials were subjected to a range of characterizations by different techniques. Subsequently, these composites were implemented as photocatalysts with a focus on decontamination of Rhodamine B and Triclopyr pollutants under the exposure of the visible light. The well crystalline and porous composite materials provided suitable sites for adsorption and accelerated the separation and transfer of photoinduced charge carriers. Introduction of Bi_2O_3 into Fe-MOF led to a significant increase in the rate of charge carrier separation at the interface. Highest degradation efficiency of 91.79% for RhB and 88.42% for TC in 120 min, respectively was exhibited by the $\text{Bi}_2\text{O}_3@$ Fe-MOF-3 under visible light illumination. The corresponding rate constants were 0.014 and 0.011 min^{-1} for RhB and TC, respectively. The acidic conditions of solution were found favorable for the removal of RhB while, in case of TC, maximum elimination of the pollutant was attained under neutral medium. Trapping experiments indicated that the holes were the dominant reactive species, followed by superoxide radicals and then hydroxyl radicals. The composite structures were inferred to be a direct Z-scheme heterojunction system. This configuration established a closely connected interface thereby promoting the efficient injection of charges, ultimately leading to the enhanced photodegradation efficiency of the composite photocatalysts.

Declaration of competing interest

The authors declare that they have no known competing financial interests or personal relationships that could have appeared to influence the work reported in this paper.

Acknowledgement

The authors extend their sincere appreciation to the Researchers Supporting Project number (RSP2023R130), King Saud University, Riyadh, Saudi Arabia for funding this research.

Appendix A. Supplementary material

Supplementary data to this article can be found online at <https://doi.org/10.1016/j.jksus.2023.102922>.

References

- Astuti, Y., Andianingrum, R., Arnelli, Haris, A., Darmawan, A., 2020a. The role of $\text{H}_2\text{C}_2\text{O}_4$ and Na_2CO_3 as precipitating agents on the physicochemical properties and photocatalytic activity of bismuth oxide. *Open Chem.* 18, 129–137. <https://doi.org/10.1515/chem-2020-0013>.
- Astuti, Y., Elesta, P.P., Widodo, D.S., Widiyandari, H., Balgis, R., 2020b. Hydrazine and urea Fueled-solution combustion method for Bi_2O_3 synthesis: characterization of physicochemical properties and photocatalytic activity. *Bull. Chem. React. Eng. Catal.* 15, 104–111. <https://doi.org/10.9767/brec.15.1.5483.104-111>.
- Chawla, A., Sudhaik, A., Sonu, Raizada, P., Ahamad, T., Le, Q.V., Nguyen, V.-H., Thakur, S., Mishra, A.K., Selvasembian, R., Singh, P., 2023. Bi-rich $\text{Bi}_2\text{O}_3/\text{Br}_2$ -based photocatalysts for energy conversion and environmental remediation: A review. *Coord. Chem. Rev.* 491, 215246 <https://doi.org/10.1016/j.ccr.2023.215246>.
- Chen, X., Dai, J., Shi, G., Li, L., Wang, G., Yang, H., 2015. Visible light photocatalytic degradation of dyes by β - Bi_2O_3 /graphene nanocomposites. *J. Alloy. Compd.* 649, 872–877. <https://doi.org/10.1016/j.jallcom.2015.05.096>.
- Chen, Y., Zhai, B., Liang, Y., Li, Y., 2020. Hybrid photocatalysts using semiconductor/MOF/graphene oxide for superior photodegradation of organic pollutants under visible light. *Mater. Sci. Semicond. Process.* 107, 104838 <https://doi.org/10.1016/j.mssp.2019.104838>.
- Cheng, L., Xie, M., Sun, Y., Liu, H., 2022. Bi_2WO_6 -wrapped 2D Ni-MOF sheets with significantly improved photocatalytic activity by a direct Z-scheme electron transfer. *J. Alloy. Compd.* 896, 163055 <https://doi.org/10.1016/j.jallcom.2021.163055>.
- Danish, M., Muneer, M., 2021. Facile synthesis of highly efficient $\text{Co}@$ ZnS QDs/g-C $_3$ N $_4$ /MWCNT nanocomposites and their photocatalytic potential for the degradation of RhB dye: Efficiency, degradation kinetics, and mechanism pathway. *Ceram. Int.* 47, 13043–13056. <https://doi.org/10.1016/j.ceramint.2021.01.168>.
- Dutta, V., Sudhaik, A., Sonu, Raizada, P., Singh, A., Ahamad, T., Thakur, S., Le, Q.V., Nguyen, V.-H., Singh, P., 2023. Tailoring S-scheme-based carbon nanotubes (CNTs) mediated Ag-Cu $\text{Bi}_2\text{O}_4/\text{Bi}_2\text{S}_3$ nanomaterials for photocatalytic dyes degradation in the aqueous system. *J. Mater. Sci. Technol.* 162, 11–24. <https://doi.org/10.1016/j.jmst.2023.03.037>.
- Fan, X., Hua, N., Jia, H., Zhu, Y., Wang, Z., Xu, J., Wang, C., 2014. Synthesis and evaluation of visible-light photocatalyst: nitrogen-doped $\text{TiO}_2/\text{Bi}_2\text{O}_3$ heterojunction structures. *Sci. Adv. Mater.* 6, 1892–1899. <https://doi.org/10.1166/sam.2014.1962>.
- Gegeel, C., Simsek, U.B., Gozmen, B., Turabik, M., 2019. Comparison of MIL-101(Fe) and amine-functionalized MIL-101(Fe) as photocatalysts for the removal of imidacloprid in aqueous solution. *J. Iran. Chem. Soc.* 16, 1735–1748. <https://doi.org/10.1007/s13738-019-01647-w>.
- Ghourchian, F., Motakef-Kazemi, N., Ghasemi, E., Ziyadi, H., 2021. Zn-based MOF-chitosan- Fe_3O_4 nanocomposite as an effective nano-catalyst for azo dye degradation. *J. Environ. Chem. Eng.* 9, 106388 <https://doi.org/10.1016/j.jece.2021.106388>.
- Guo, W., Chen, Z., Yang, C., Neumann, T., Kübel, C., Wenzel, W., Welle, A., Pflöging, W., Shekha, O., Wöll, C., Redel, E., 2016. Bi_2O_3 nanoparticles encapsulated in surface mounted metal-organic framework thin films. *Nanoscale* 8, 6468–6472. <https://doi.org/10.1039/C6NR00532B>.
- Hao, C., Chen, F., Bian, K., Tang, Y., Shi, W., 2022. Spindle-like MIL101(Fe) decorated with Bi_2O_3 nanoparticles for enhanced degradation of chlortetracycline under visible-light irradiation. *Beilstein J. Nanotechnol.* 13, 1038–1050. <https://doi.org/10.3762/bjnano.13.91>.
- Hu, L., Chen, J., Wei, Y., Wang, M., Xu, Y., Wang, C., Gao, P., Liu, Y., Liu, C., Song, Y., Ding, N., Liu, X., Wang, R., 2023. Photocatalytic degradation effect and mechanism of Karenia mikimotoi by non-noble metal modified TiO_2 loading onto copper metal organic framework (SNP- $\text{TiO}_2@$ Cu-MOF) under visible light. *J. Hazard. Mater.* 442, 130059 <https://doi.org/10.1016/j.jhazmat.2022.130059>.
- Hu, Z., Zhou, J., Zhang, Y., Liu, W., Zhou, J., Cai, W., 2018. The formation of a direct Z-scheme $\text{Bi}_2\text{O}_3/\text{MoO}_3$ composite nanocatalyst with improved photocatalytic activity under visible light. *Chem. Phys. Lett.* 706, 208–214. <https://doi.org/10.1016/j.cplett.2018.06.006>.
- Iyyapushpam, S., Nishanthi, S.T., Pathinettam Padiyan, D., 2013. Photocatalytic degradation of methyl orange using α - Bi_2O_3 prepared without surfactant. *J. Alloy. Compd.* 563, 104–107. <https://doi.org/10.1016/j.jallcom.2013.02.107>.
- Joseph, J., Iftikhar, S., Srivastava, V., Fallah, Z., Zare, E.N., Sillanpää, M., 2021. Iron-based metal-organic framework: Synthesis, structure and current technologies for water reclamation with deep insight into framework integrity. *Chemosphere* 284, 131171. <https://doi.org/10.1016/j.chemosphere.2021.131171>.
- Khan, A.A.P., Sonu, Sudhaik, A., Raizada, P., Khan, A., Rub, M.A., Azum, N., Alotaibi, M. M., Singh, P., Asiri, A.M., 2023. AgI coupled $\text{SiO}_2@$ Cu Fe_2O_4 novel photocatalytic nano-material for photo-degradation of organic dyes. *Catal. Commun.* 179, 106685 <https://doi.org/10.1016/j.catcom.2023.106685>.
- Koli, P.B., Shinde, S.G., Kapadnis, K.H., Patil, A.P., Shinde, M.P., Khairnar, S.D., Sonawane, D.B., Ingale, R.S., 2021. Transition metal incorporated, modified bismuth oxide (Bi_2O_3) nano photo catalyst for deterioration of rosaniline hydrochloride dye as resource for environmental rehabilitation. *J. Indian Chem. Soc.* 98, 100225 <https://doi.org/10.1016/j.jics.2021.100225>.
- Kumari, V., Yadav, S., Jindal, J., Sharma, S., Kumari, K., Kumar, N., 2020. Synthesis and characterization of heterogeneous ZnO/CuO hierarchical nanostructures for photocatalytic degradation of organic pollutant. *Adv. Powder Technol.* 31, 2658–2668. <https://doi.org/10.1016/j.apt.2020.04.033>.
- Lan, Q., Jin, S., Yang, B., Zhang, Z., Li, X., Xie, H., Jin, X., Zhang, H., Zhao, Q., 2022. Filling polyoxoanions into MIL-101(Fe) for adsorption of organic pollutants with facile and complete visible light photocatalytic decomposition. *Molecules* 27, 3404. <https://doi.org/10.3390/molecules27113404>.
- Li, J., Wang, L., Liu, Y., Zeng, P., Wang, Y., Zhang, Y., 2020. Removal of Berberine from Wastewater by MIL-101(Fe): Performance and Mechanism. *ACS Omega* 5, 27962–27971. <https://doi.org/10.1021/acsomega.0c03422>.
- Liu, S., Jiang, X., Waterhouse, G.I.N., Zhang, Z.-M., Yu, L., 2021. Construction of Z-scheme Titanium-MOF/plasmonic silver nanoparticle/NiFe layered double hydroxide photocatalysts with enhanced dye and antibiotic degradation activity under visible light. *Sep. Purif. Technol.* 278, 119525 <https://doi.org/10.1016/j.seppur.2021.119525>.
- Motakef-Kazemi, N., Yagoubi, M., 2020. Green synthesis and characterization of bismuth oxide nanoparticle using mentha pulegium extract. *IJPR*. <https://doi.org/10.22037/ijpr.2019.15578.13190>.
- Nguyen, V., Nguyen, T., Bach, L., Hoang, T., Bui, Q., Tran, L., Nguyen, C., Vo, D.-V., Do, S., 2018. Effective photocatalytic activity of mixed Ni/Fe-base metal-organic framework under a compact fluorescent daylight lamp. *Catalysts* 8, 487. <https://doi.org/10.3390/catal8110487>.
- Nguyen Thi, H.-T., Tran Thi, K.-N., Hoang, N.B., Tran, B.T., Do, T.S., Phung, C.S., Nguyen Thi, K.-O., 2021. Enhanced degradation of rhodamine B by metallic organic frameworks based on NH_2 -MIL-125(Ti) under visible light. *Materials* 14, 7741. <https://doi.org/10.3390/ma14247741>.

- Poulios, I., Kositzki, M., Kouras, A., 1998. Photocatalytic decomposition of triclopyr over aqueous semiconductor suspensions. *J. Photochem. Photobiol. A Chem.* 115, 175–183. [https://doi.org/10.1016/S1010-6030\(98\)00259-7](https://doi.org/10.1016/S1010-6030(98)00259-7).
- Raizada, P., Sudhaik, A., Singh, P., Hosseini-Bandegharaei, A., Thakur, P., 2019. Converting type II AgBr/VO into ternary Z scheme photocatalyst via coupling with phosphorus doped g-C₃N₄ for enhanced photocatalytic activity. *Sep. Purif. Technol.* 227, 115692 <https://doi.org/10.1016/j.seppur.2019.115692>.
- Sharma, S., Kumar, N., Mari, B., Chauhan, N.S., Mittal, A., Maken, S., Kumari, K., 2021. Solution combustion synthesized TiO₂/Bi₂O₃/CuO nano-composites and their photocatalytic activity using visible LEDs assisted photoreactor. *Inorg. Chem. Commun.* 125, 108418 <https://doi.org/10.1016/j.inoche.2020.108418>.
- Tang, Y., Yin, X., Mu, M., Jiang, Y., Li, X., Zhang, H., Ouyang, T., 2020. Anatase TiO₂@MIL-101(Cr) nanocomposite for photocatalytic degradation of bisphenol A. *Colloids Surf. A Physicochem. Eng. Asp* 596, 124745. <https://doi.org/10.1016/j.colsurfa.2020.124745>.
- Wu, B., Sun, T., Liu, N., Lu, L., Zhang, R., Shi, W., Cheng, P., 2022. Modulation of Z-scheme heterojunction interface between ultrathin C₃N₅ nanosheets and metal-organic framework for boosting photocatalysis. *ACS Appl. Mater. Interfaces* 14, 26742–26751. <https://doi.org/10.1021/acsami.2c04729>.
- Yan, D., Hu, H., Gao, N., Ye, J., Ou, H., 2019. Fabrication of carbon nanotube functionalized MIL-101(Fe) for enhanced visible-light photocatalysis of ciprofloxacin in aqueous solution. *Appl. Surf. Sci.* 498, 143836 <https://doi.org/10.1016/j.apsusc.2019.143836>.
- Yang, J., Xie, T., Liu, C., Xu, L., 2018. Facile fabrication of dumbbell-Like β-Bi₂O₃/graphene nanocomposites and their highly efficient photocatalytic activity. *Materials* 11, 1359. <https://doi.org/10.3390/ma11081359>.
- Zhong, X., Zhu, Y., Sun, Q., Jiang, M., Li, J., Yao, J., 2022. Tunable Z-scheme and Type II heterojunction of Cu_xO nanoparticles on carbon nitride nanotubes for enhanced visible-light ammonia synthesis. *Chem. Eng. J.* 442, 136156 <https://doi.org/10.1016/j.cej.2022.136156>.